Supplement of

Linking global terrestrial CO_2 fluxes and environmental drivers using OCO-2 and a geostatistical inverse model

Zichong Chen et al.

Correspondence to: Zichong Chen (zchen74@jhu.edu)

S1. Additional detail on covariance parameter optimization

We use Restricted Maximum Likelihood (RML; e.g., *Kitanidis*, 1997; *Gourdji et al*., 2012; *Miller et al*., 2016) to estimate the covariance parameters that define **Q**, including the variance of **Q** (referred to as σ_Q^2), the decorrelation length (*l*), and the decorrelation time (*t*) (Table S1). We iteratively optimize these covariance parameters using flux data from CarbonTracker (CT2017, *Peters et al*., 2007, *https://www.esrl.noaa.gov/gmd/ccgg/carbontracker/*). Here we assume that the spatial and temporal properties of CO_2 fluxes from CT2017 are a reasonable proxy for the covariance parameters that should be used in the GIM. Several previous studies have also used this proxy approach to estimate covariance parameters in the inverse model (e.g., *Mueller et al*., 2008; *Gourdji et al*., 2008, 2010, 2012). Note that we estimate the parameters for land and ocean separately. The terrestrial flux estimate from CT2017 includes several flux types, i.e., biospheric, fossil fuel and biomass burning fluxes. We sum all of these flux types and apply RML to the total terrestrial flux. All the flux data from CT2017 are re-gridded to 4^o latitude by 5^o longitude spatial and daily temporal resolution before applying RML, consistent with our GIM setup. Note that variances estimated here are similar to previous, global GIM studies but the correlation lengths are shorter. Specifically, *Mueller et al. (2008)* and *Gourdji et al* (2008) estimated global CO_2 fluxes for years 1997 to 2001 using *in situ* CO_2 observations and a GIM. They estimated a variance (σ_Q^2) of 0.40 and 0.28 (μmol/m^2/s)^2 for land regions, respectively, and a variance of 0.003 (μmol/m^2/s)^2 for oceans, roughly similar to the numbers here. By contrast, they estimated correlation lengths of 5400 and 8100 km, respectively, for land regions and 17,100 km for oceans. Note that those studies used an exponential covariance model, and the exponential correlation length parameters listed in those studies are equal to one-third of the full correlation lengths listed above. By contrast, the full correlation length and correlation length parameter (*l*) are the same for the spherical model used here. *Mueller et al. (2008)* and *Gourdji et al* (2008) estimated global CO_2 fluxes using an *in situ* network that was geographically sparse compared to the current OCO-2 observations, and the long correlation lengths used in those studies were likely helpful for interpolating CO_2 fluxes in regions with poor observational constraints. By contrast, the shorter correlation lengths estimated in this study are likely more appropriate given the greater spatial density of OCO-2 observations relative to the *in situ* network at the turn of the century.

We further construct **R** as a diagonal matrix with constant elements on the diagonal, and here we use values for **R** from existing literature (*Miller et al*., 2018). *Miller et al* (2018) evaluated when and where the OCO-2 observations can constrain biospheric flux variability. As part of that study, the authors estimated a variance for **R** of (1.19 ppm)^2.

Table S1. *Estimated covariance matrix parameters using a spherical covariance model*

Covariance parameters	σ_Q^2 ((μmol/m^2/s)^2)	*l* (km)	*t* (days)
Land	0.3	1876	5.7
Ocean	0.012	5013	8.2

S2. Scaled temperature function

Most terrestrial biosphere models (TBMs) estimate CO_2 fluxes as a nonlinear or piecewise function of temperature (e.g., *Randerson et al*., 1997; *Thornton et al*., 2009; *Dayalu et al*., 2018). In this study, we use a scaled function of temperature from the Vegetation Photosynthesis and Respiration Model (VPRM, *Mahadevan et al*., 2008; *Dayalu et al*., 2018) as an environmental driver in the inverse model (in **X**, Eq. 1). This function peaks at the optimal temperature for photosynthesis and declines at higher and lower temperatures:

$$\boldsymbol{T_{scale}} = \frac{(\boldsymbol{T_{air}} - \boldsymbol{T_{min}})(\boldsymbol{T_{air}} - \boldsymbol{T_{max}})}{(\boldsymbol{T_{air}} - \boldsymbol{T_{min}})(\boldsymbol{T_{air}} - \boldsymbol{T_{max}}) - (\boldsymbol{T_{air}} - \boldsymbol{T_{opt}})^2} \qquad \text{(S1)}$$

The scaled temperature ($\boldsymbol{T_{scale}}$) is calculated based on a minimum ($\boldsymbol{T_{min}}$ = 0 ^{o}C) and maximum ($\boldsymbol{T_{max}}$ = 40 ^{o}C) temperature threshold and an optimal temperature ($\boldsymbol{T_{opt}}$) for photosynthesis which is set for each biome. In this study, we follow existing literature (*Mahadevan et al*., 2008; *Luus et al*., 2017; *Dayalu et al*., 2018) and set an optimal temperature of 15 ^{o}C for tundra and boreal biomes, and 20 ^{o}C for temperate, tropical, and desert/shrubland biomes. An example of scaled temperature as a function of air temperature over the temperate forest biome is illustrated in Fig. S1.

S3. Additional detail on the Bayesian Information Criterion (BIC)

We evaluate a total of 5,366 combinations of environmental drivers using model selection, and Table S2 lists 10 combinations of environmental drivers with the lowest BIC scores. The BIC rewards combinations of environmental drivers in **X** that better reproduce OCO-2 observations and penalizes combinations with many environmental drivers to prevent overfitting; the best combination of environmental drivers is the combination with the lowest score. Note that the branch and bound algorithm used here (*Yadav et al*., 2013) is designed to minimize the number of combinations that need to be evaluated to find the combination with the lowest BIC score. As a result, Table S2 is not exhaustive and only lists the top 10 combinations among those evaluated.

The differences in BIC scores among models provides a way of evaluating evidence for or against each model. Previous studies (e.g., *Kass and Raftery*, 1995; *Raftery*, 1995) suggested that differences in BIC scores from 0 to 2, 2 to 6, 6 to 10, and larger than 10 indicate weak, positive, strong and very strong evidence, respectively, for the lower-scoring model. For example, the difference in BIC scores between the best and 2^{nd}-best models is 1, indicating weak evidence for the best model over the 2^{nd}-best model (*Kass and Raftery*, 1995). The 2^{nd}-best model includes two additional drivers than the best model -- scaled temperature in temperate grasslands and in temperate forests. However, these additional environmental drivers play a very small role in the deterministic model; the estimated $\boldsymbol{\beta}$ values assigned to scaled temperature from temperate grasslands and from temperate forests are very small (i.e., -0.04 and -0.07, respectively). By contrast, the difference in BIC scores between the best model and 10^{th}-best model is 8, suggesting strong evidence in favor of the best model over the 10^{th}-best model.

Most of the models in positions 2 through 10 in Table S2 contain more variables than the best model. Many of these models include scaled temperature for temperate biomes and many include soil moisture for the desert/shrubland biome. For example, we select four more drivers in the 10^{th}-best model than in the best model. These additional environmental drivers in models 2 through 10 result in a larger penalty term in the BIC, and that penalty is greater than the improvement in model-data fit due to the inclusion of additional drivers.

Table S2. *Combinations of environmental drivers with the lowest BIC scores*

Model	Selected Environmental drivers*						Number of selected environmental drivers	BIC Score	BIC difference
	Boreal forests	Temperate grasslands	Temperate forests	Tropical grasslands	Tropical forests	Deserts/shrublands			
1 (the best model)	PAR	Precip; PAR	Precip; PAR	Precip; Scaled Temp	Precip; Scaled Temp; PAR	Precip; Scaled Temp	12	10217	0
2	PAR	Precip; PAR; Scaled Temp	Precip; PAR; Scaled Temp	Precip; Scaled Temp	Precip; Scaled Temp; PAR	Precip; Scaled Temp	14	10218	1
3	PAR	Precip; PAR; Scaled Temp	Precip; PAR; Scaled Temp	Precip; Scaled Temp	Precip; Scaled Temp; PAR	Precip; Scaled Temp Soil moist	15	10219	2
4	PAR	Precip; PAR	Precip; PAR; Scaled Temp	Precip; Scaled Temp	Precip; Scaled Temp; PAR	Precip; Scaled Temp	13	10220	3
5	PAR	Precip; PAR; Scaled Temp	Precip; PAR	Precip; Scaled Temp	Precip; Scaled Temp; PAR	Precip; Scaled Temp	13	10221	4
6	PAR	Precip; PAR; Scaled Temp	Precip; PAR; Scaled Temp	Precip; Scaled Temp	Precip; Scaled Temp; PAR	Precip; Scaled Temp; PAR	15	10224	7
7	PAR	Precip; PAR	Precip; PAR; Scaled Temp	Precip; Scaled Temp	Precip; Scaled Temp; PAR	Precip; Scaled Temp; Soil moist	14	10224	7
8	PAR	PAR	Precip; PAR	Precip; Scaled Temp	Precip; Scaled Temp; PAR	Precip; Scaled Temp	11	10225	8
9	PAR	Precip; PAR; Scaled Temp	Precip; PAR; Scaled Temp	Precip; Scaled Temp	Precip; Scaled Temp; PAR	Precip; Scaled Temp; Soil moist; PAR	16	10225	8
10	PAR	Precip; PAR; Scaled Temp	Precip; PAR; Scaled Temp	Precip; Scaled Temp; PAR	Precip; Scaled Temp; PAR	Precip; Scaled Temp; Soil moist	16	10225	8

*Precip, Scaled Temp, and Soil moist denote daily precipitation, scaled temperature, and soil moisture, respectively.

S4. Additional detail on the reduced-rank approximation approach

We estimate the posterior uncertainties using a reduced rank algorithm (e.g., *Saibaba and Kitanid*is, 2015; *Miller et al.* 2019). This algorithm is computationally feasible even for very large inverse problems; it uses a reduced rank approximation of a matrix product to improve the computational efficiency of the uncertainty calculations. The more eigenpairs used in this approximation, the more accurate the uncertainty estimate. Fig. S2 displays the estimated posterior uncertainties as a function of the number of eigenpairs used in the reduced rank approach. In brief, we employ two forward model runs and two adjoint model runs to create each approximate eigenpair using a randomized algorithm (*Halko et al*., 2011; *Saibaba and Kitanidis*, 2015). The posterior uncertainties decrease and gradually converge toward the solution as the number of eigenpairs increases. In this particular study, the posterior uncertainties begin to asymptote toward a stable value when the number of eigenpairs approaches 90. To be safe, we use 100 eigenpairs to estimate the uncertainties in this study.

S5. Additional detail on the posterior uncertainty estimate for biospheric fluxes

We estimate biospheric fluxes as the difference between the posterior flux estimate and the flux patterns that map onto the ODIAC fossil fuel inventory, $\boldsymbol{s} - \boldsymbol{X_{ff}}\beta_{ff}$. $\boldsymbol{X_{ff}}$ (*m* × *1*) is the column associated with fossil fuel emissions included in **X**, and β_{ff} is the drift coefficient for fossil fuel emissions.

We also estimate the uncertainty in this biospheric contribution (Table 2 and Figure 5). These uncertainty calculations require calculating the posterior covariance of both $\boldsymbol{s}$ and $\boldsymbol{\beta}$ (e.g., *Michalak et al*., 2004; *Saibaba and Kitanidis*, 2015):

$$\begin{bmatrix} \mathbf{V_s} & \mathbf{V_{s\beta}} \\ \mathbf{V_{\beta s}} & \mathbf{V_\beta} \end{bmatrix} = \begin{bmatrix} (\mathbf{Q^{-1}} + \mathbf{H^T}(\mathbf{R^{-1}H}) & -\mathbf{Q^{-1}X} \\ -\mathbf{X^TQ^{-1}} & \mathbf{X^TQ^{-1}X} \end{bmatrix}^{-1} \qquad \text{(S2)}$$

where $\mathbf{V_s}$ (*m* × *m*), $\mathbf{V_\beta}$ (*p* × *p*), $\mathbf{V_{s\beta}}$ (*m* × *p*), and $\mathbf{V_{\beta s}}$ (*p* × *m*) is the posterior covariance of $\boldsymbol{s}$, the posterior covariance of $\boldsymbol{\beta}$, the posterior covariance of $\boldsymbol{s}$ and $\boldsymbol{\beta}$, and the posterior covariance of $\boldsymbol{\beta}$ and $\boldsymbol{s}$, respectively. It is not computationally feasible to directly calculate Eq. S2 due to the size of the matrix inverse on the right-hand side. Hence, we take the inverse of the matrices in Eq. S2 using the properties of a block matrix (e.g., *Lu and Shiou*, 2002; *Saibaba and Kitanidis*, 2015) and then substitute the equations for the matrices $\mathbf{V_1}$, $\mathbf{V_2}$, and $\mathbf{V_3}$ (Eqs. 5-7) into the expression of

$\mathbf{V_s}$, $\mathbf{V_\beta}$, $\mathbf{V_{s\beta}}$, and $\mathbf{V_{\beta s}}$:

$$\mathbf{V_s} = \mathbf{V_1} + \mathbf{V_2}\mathbf{V_3}\mathbf{V_2^T} \tag{S3}$$

$$\mathbf{V_\beta} = \mathbf{V_3} \tag{S4}$$

$$\mathbf{V_{s\beta}} = \mathbf{V_2}\mathbf{V_3} \tag{S5}$$

$$\mathbf{V_{\beta s}} = \mathbf{V_3}\mathbf{V_2^{\mathit{T}}} \tag{S6}$$

Following the variance sum law, we estimate the posterior uncertainty for biospheric fluxes ($\mathbf{V}_{\mathbf{s}-X_{ff}\beta_{ff}}$, dimensions $m \times m$):

$$\mathbf{V}_{\mathbf{s}-X_{ff}\beta_{ff}} = \mathbf{V_s} + \boldsymbol{X_{ff}} V_{\beta,ff} \boldsymbol{X_{ff}^T} - 2\boldsymbol{V_{s\beta,ff}}\boldsymbol{X_{ff}^T} \tag{S7}$$

where $V_{\beta,ff}$ (1×1) is the covariance matrix of $\boldsymbol{\beta}$ associated with fossil fuel emissions (β_{ff}), $\boldsymbol{V_{s\beta,ff}}$ ($m \times 1$) is the covariance of $\boldsymbol{s}$ and β_{ff}.

S6. Sensitivity analysis on the impact of biomass burning and ocean fluxes in the model selection

We do not select biomass burning emissions from the Global Fire Emissions Database (GFED) version 4.1 (*Randerson et al*., 2018) or ocean fluxes from *Takahashi et al*. (2016) using the BIC. This result suggests that neither biomass burning fluxes from GFED nor ocean fluxes from *Takahashi et al*. (2016) help reproduce the OCO-2 observations more than the penalty term in the BIC (Sect. 2.5).

Indeed, we construct a sensitivity test to examine the impact of GFED and ocean fluxes from *Takahashi et al*. (2016) on the model selection. In the sensitivity test, we only evaluate combinations of variables for **X** that include biomass burning emissions from GFED and ocean fluxes from *Takahashi et al*. (2016) (Table S3). The sensitivity test shows that the inclusion of GFED and/or ocean fluxes from *Takahashi et al*. (2016) in **X** yields much larger BIC scores (>10) relative to formulations of **X** that do not include these variables (Table S3). Furthermore, the inverse model assigns negative $\boldsymbol{\beta}$ values to GFED and ocean fluxes from *Takahashi et al*. (2016). Evidently, the OCO-2 observations are not sufficient to constrain physically realistic coefficients ($\boldsymbol{\beta}$) for these variables. Moreover, the negative $\boldsymbol{\beta}$ values associated with GFED and ocean fluxes from *Takahashi et al*. (2016) will potentially introduce spurious noise into the flux estimate and therefore do not help reproduce the OCO-2 observations.

Table S3. The impact of biomass burning fluxes from GFED and ocean fluxes from *Takahashi et al.* (2016) on BIC scores calculated in model selection.

Case scenarios	GFED fluxes are always included in **X**	Ocean fluxes from *Takahashi et al*. (2016) are always included in **X**	Both GFED and ocean fluxes from *Takahashi et al*. (2016) are always included in **X**	No requirement that GFED or *Takahashi et al.* (2016) is included in **X**.
Lowest BIC score	10298	10275	10284	10217

S7. Comparison of posterior atmospheric CO_2 concentrations and aircraft-*based in situ* observations

We pass the posterior fluxes (***s***, Figure 2c) through the transport model (GEOS-Chem) to estimate atmospheric CO_2 and compare this estimate with aircraft observations of CO_2. We obtain aircraft data from the GLOBALVIEW+ package (Version 5.0, Cooperative Global Atmospheric Data Integration Project, 2019) and the National Institute for Space Research (INPE) ObsPack data product (version 2.0, NOAA Carbon Cycle Group ObsPack Team, 2018; Masarie et al., 2014). Here we compare against aircraft observations from six sampling sites (Table S4) across boreal, temperate and tropical regions. We do not compare against aircraft observations from sites that are on or off the coast of continents (e.g., Offshore Cape May, New Jersey, USA (CMA), or Offshore Corpus Christi, Texas, USA (TGC)), as it is difficult to simulate atmospheric CO_2 for coastal sites given relatively coarse spatial resolution of GEOS-Chem (i.e., 4^{o} latitude × 5^{o} longitude in this study). We also do not use aircraft data with very limited temporal coverage. For example, there are only two months of available observations at West Branch, Iowa, USA (WBI) and Homer, Illinois, USA (HIL) in year 2016. We further compare modeled and measured aircraft observations both above and below 3000 masl., consistent with the set up in *Crowell et al* (2019).

Modeled CO_2 mixing ratios agree closely with aircraft observations (Figs. S5 and S6). For aircraft observations above 3000 masl. (Fig. S5), the biases between modeled and observed CO_2 mixing ratios are small (i.e., -0.33 to 0.14 ppm), and the root-mean-square errors (RMSEs) range from 0.63 to 1.04 ppm. For aircraft observations below 3000 masl (Fig. S6), there are larger model-data biases (i.e., -0.37 to 0.82 ppm) than those above 3000 masl, but the biases reported here are nevertheless broadly consistent with comparisons in the recent MIP study (*Crowell et al.*, 2019). This agreement between modeled and observed CO_2 implies an absence of major biases in the GIM flux estimate. *Crowell et al* (2019) provide further comparisons between CO_2 flux estimates derived from OCO-2 and global *in situ* CO_2 observations.

Table S4. *Regular aircraft monitoring sites used in this study*

Site code	Location	Longitude	Latitude	Network
PFA	Poker Flat, Alaska, USA	-148.76	64.90	NOAA/ESRL Global Greenhouse Gas Reference Network (e.g., *Sweeny et al.*, 2015)
ETL	East Trout Lake, Saskatchewan, Canada	-104.99	54.35	
SGP	Southern Great Plains, Oklahoma, USA	-97.49	36.61	
LEF	Park Falls, Wisconsin, USA	-90.27	45.95	
ALF	Alta Floresta, Brazil	-56.79	-8.92	INPE
RBA	Rio Branco, Brazil	-67.6	-9.36	

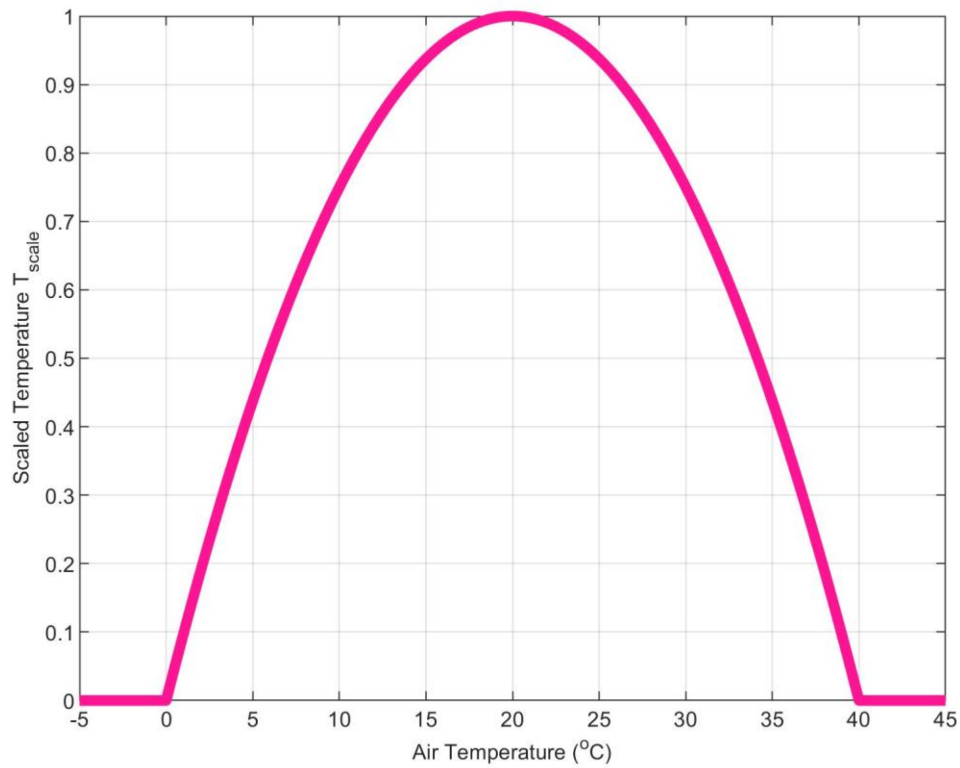

Figure S1. Scaled air temperature function for photosynthesis. This figure displays the function used for the temperate forest biome; the function has different optimal temperatures in different biomes.

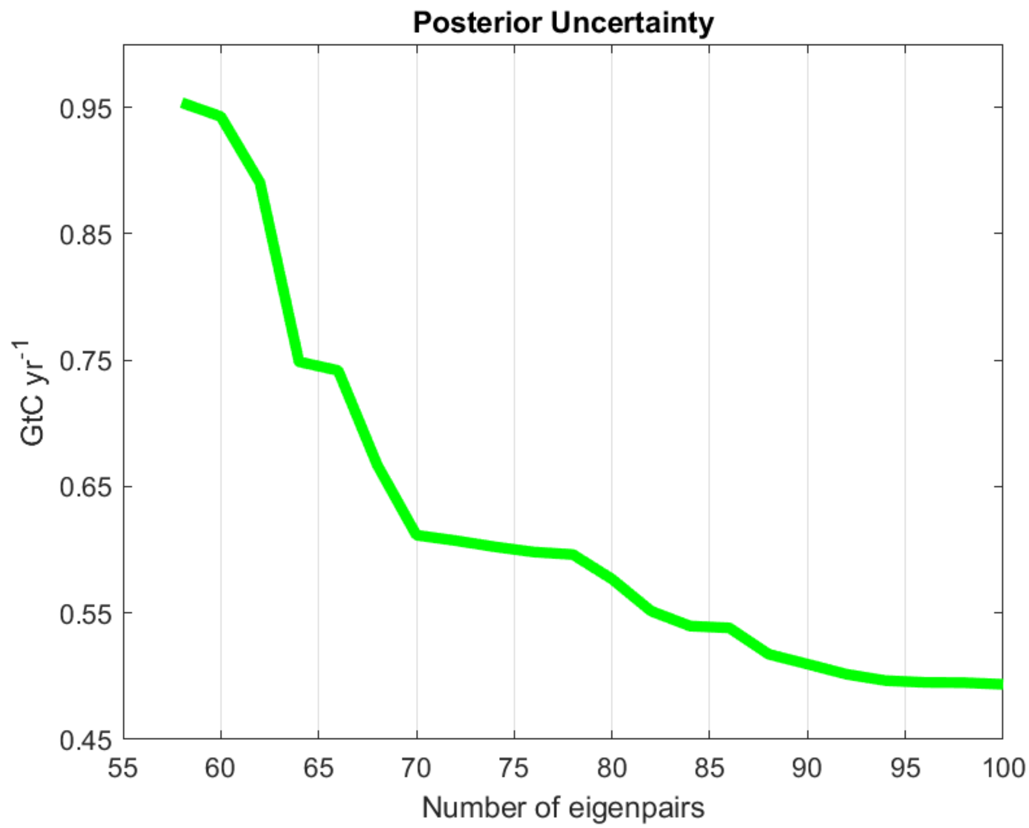

Figure S2. Estimated posterior uncertainties as a function of the number of eigenpairs using the reduced rank approach. The estimated uncertainties decrease as the number of eigenpairs increases, and the uncertainty estimate flattens out when the number of eigenpairs is 90 or above.

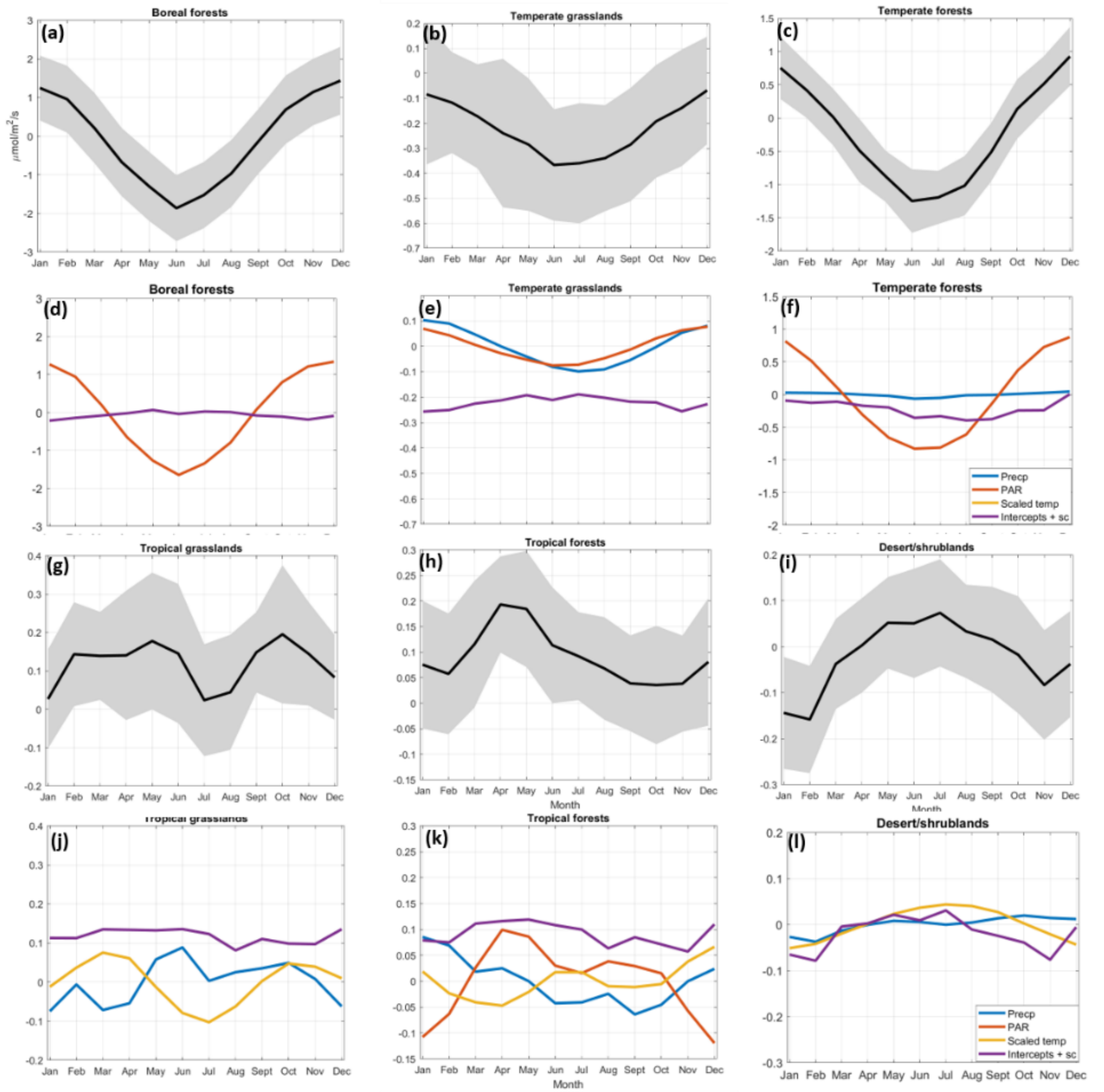

Figure S3. Monthly averaged biospheric CO_2 fluxes over (a) boreal forests, (b) temperate grasslands, (c) temperate forests, (g) tropical grasslands, (h) tropical forests, and (i) deserts/shrublands; and contributions from different environmental drivers ($\mathbf{X}\boldsymbol{\beta}$), the intercept terms and the stochastic component (ζ), respectively, to the flux estimate in each biome (d-l). Shaded areas indicate associated uncertainties with 95% confidence interval. *Precp*, *Scaled temp*, and *Intercepts + sc* denote daily precipitation, scaled temperature, and combined intercept term and stochastic component, respectively. Note we do not show the seasonal patterns over tundra because no environmental drivers are selected over tundra (Table 1). The seasonal patterns shown here is a mix of both northern and southern hemisphere within each biome. In Fig. S4 we split each biome at the Equator and show more detailed, hemispheric seasonal patterns from within each biome.

213

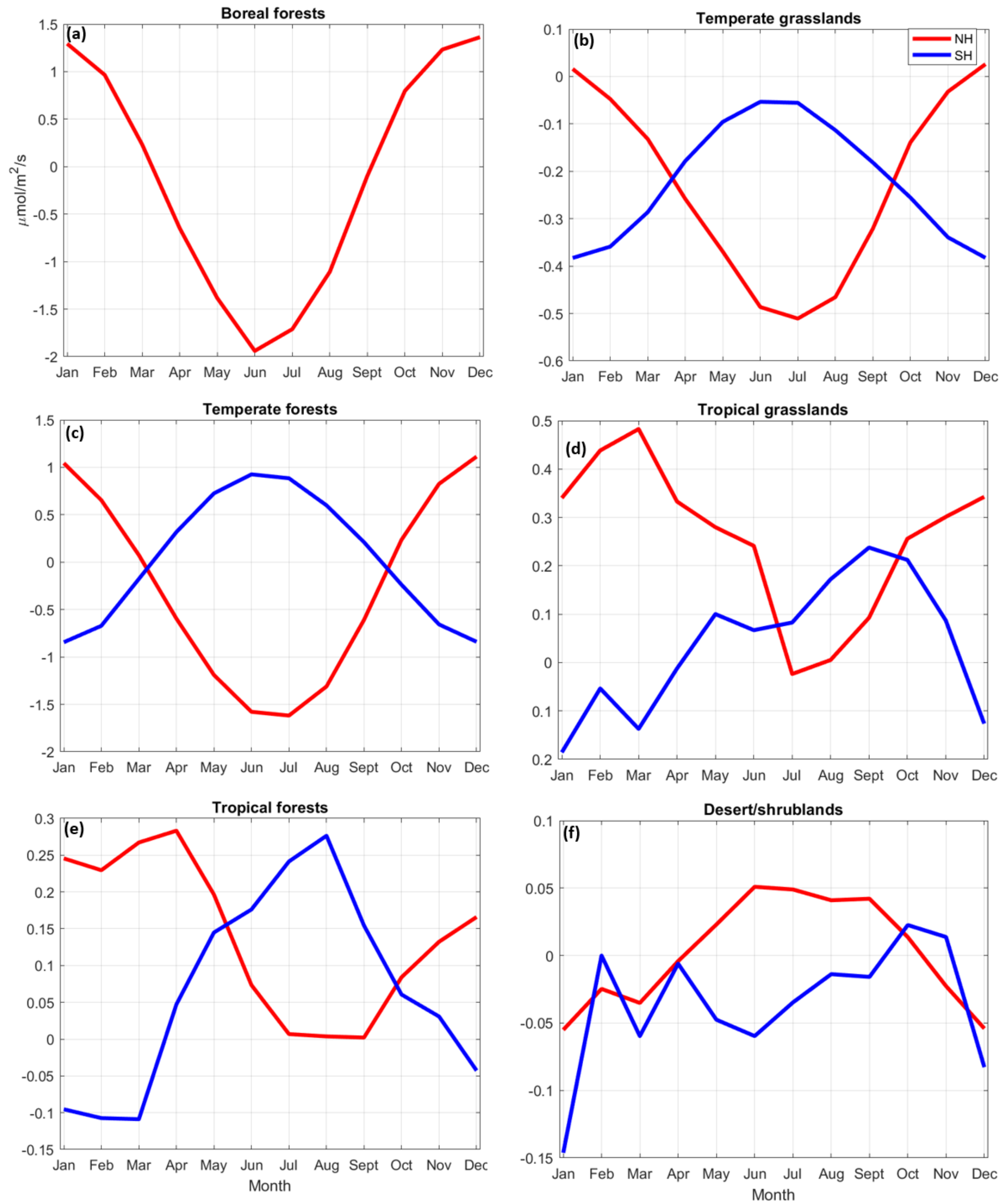

Figure S4. Monthly averaged biospheric CO_2 fluxes from the northern (red) and southern (blue) hemisphere, respectively, within each biome. Note we do not show the seasonal pattern from the southern hemisphere for boreal forests, as there is no boreal forests biome in the southern hemisphere based on the seven-biome map (Fig. 1).

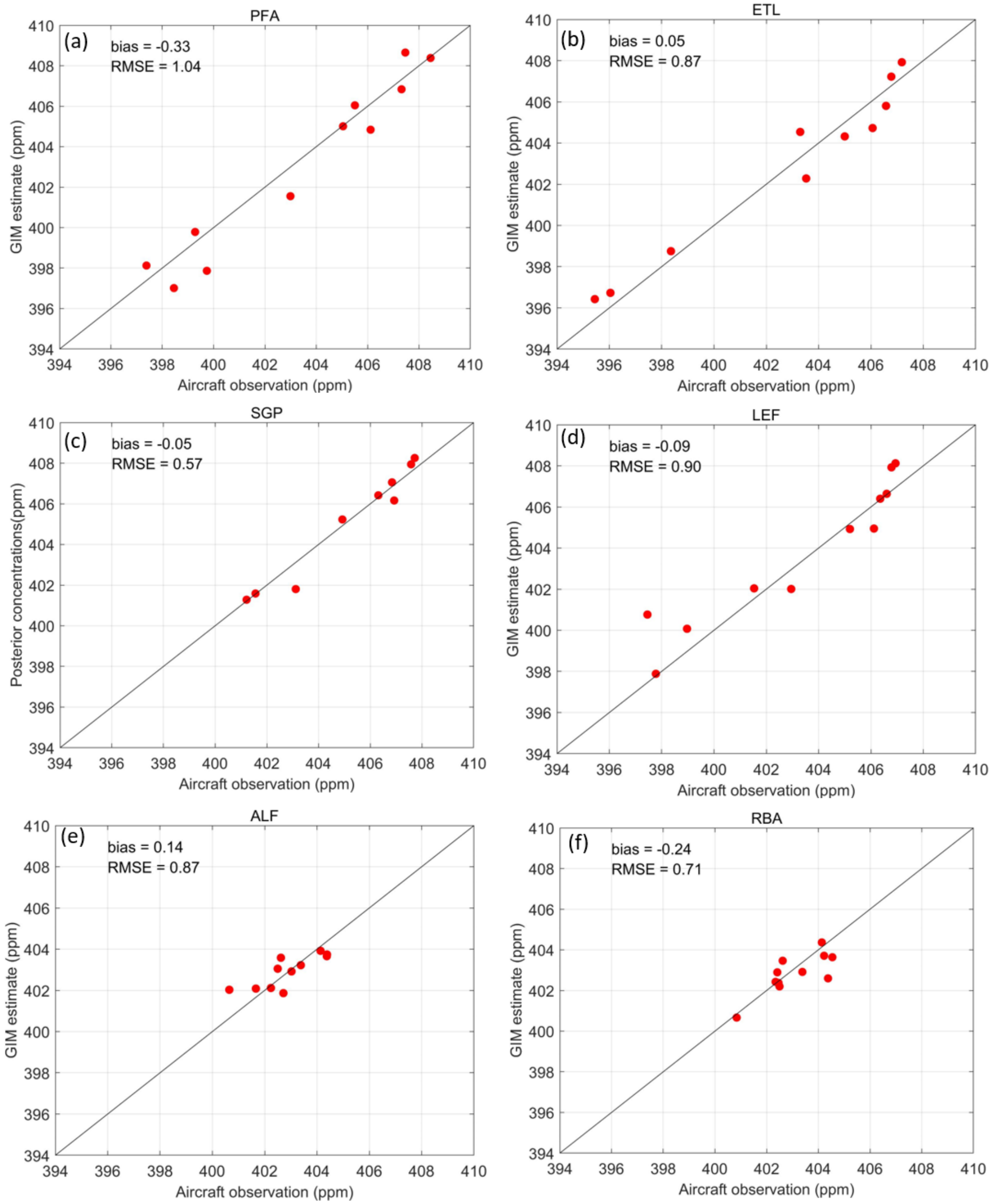

Figure S5. Comparison of modeled and observed CO_2 mixing ratios above 3000 masl. at several aircraft monitoring sites: (a) PFA, (b) ETL, (c) ESP, (d) LEF, (e) ALF, and (f) RBA.

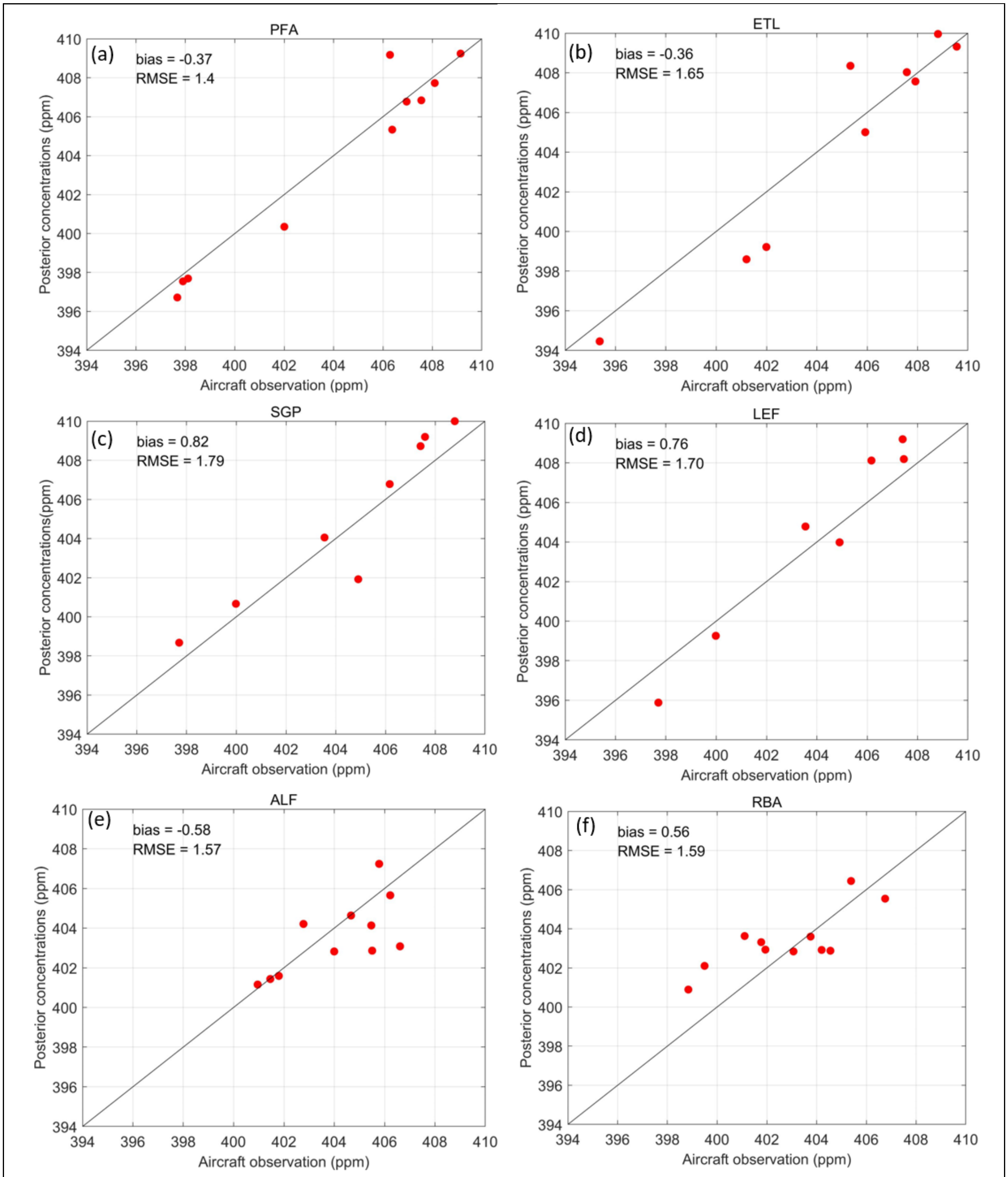

Figure S6. Comparison of modeled and observed CO_2 mixing ratios below 3000 masl. at several aircraft monitoring sites: (a) PFA, (b) ETL, (c) ESP, (d) LEF, (e) ALF, and (f) RBA.

References

Cooperative Global Atmospheric Data Integration Project (2019). Multi-laboratory compilation of atmospheric carbon dioxide data for the period 1957-2018; obspack_co2_1_GLOBALVIEWplus_v5.0_2019_08_12; NOAA Earth System Research Laboratory, Global Monitoring Division. http://dx.doi.org/10.25925/20190812.

Crowell, S., Baker, D., Schuh, A., Basu, S., Jacobson, A. R., Chevallier, F., Liu, J., Deng, F., Feng, L., McKain, K., Chatterjee, A., Miller, J. B., Stephens, B. B., Eldering, A., Crisp, D., Schimel, D., Nassar, R., O'Dell, C. W., Oda, T., Sweeney, C., Palmer, P. I., and Jones, D. B. A.: The 2015–2016 carbon cycle as seen from OCO-2 and the global in situ network, Atmos. Chem. Phys., 19, 9797–9831, https://doi.org/10.5194/acp-19-9797-2019, 2019. https://doi.org/10.5194/acp-2019-87

Dayalu, A., Munger, J. W., Wofsy, S. C., Wang, Y., Nehrkorn, T., Zhao, Y., ... & Luus, K. (2018). Assessing biotic contributions to CO 2 fluxes in northern China using the Vegetation, Photosynthesis and Respiration Model (VPRM-CHINA) and observations from 2005 to 2009. *Biogeosciences*, *15*(21), 6713-6729. https://doi.org/10.5194/bg-15-6713-2018

Gourdji, Sharon M., Mueller, K. L., Schaefer, K., & Michalak, A. M. (2008). Global monthly averaged CO2 fluxes recovered using a geostatistical inverse modeling approach: 2. Results including auxiliary environmental data . *Journal of Geophysical Research*, *113*(D21), 1–15. https://doi.org/10.1029/2007jd009733

Gourdji, S. M., Hirsch, A. I., Mueller, K. L., Yadav, V., Andrews, A. E., & Michalak, A. M. (2010). Regional-scale geostatistical inverse modeling of North American CO2 fluxes: A synthetic data study. *Atmospheric Chemistry and Physics*, *10*(13), 6151–6167. https://doi.org/10.5194/acp-10-6151-2010

Gourdji, S. M., et al. (2012), North American CO2 exchange: Inter-comparison of modeled estimates with results from a fine-scale atmospheric inversion, *Biogeosciences*, *9*(1), 457–475, doi:10.5194/bg-9-457-2012.

Halko, N., Martinsson, P. G., & Tropp, J. A. (2011). Finding structure with randomness: Probabilistic algorithms for constructing approximate matrix decompositions. *SIAM review*, *53*(2), 217-288. https://doi.org/10.1137/090771806

Saibaba, A. K. and Kitanidis, P. K. (2015). Fast computation of uncertainty quantification measures in the geostatistical approach to solve inverse problems, *Adv. Water Resour.*, 82, 124 – 138, https://doi.org/10.1016/j.advwatres.2015.04.012

Peters, W., Jacobson, A. R., Sweeney, C., Andrews, A. E., Conway, T. J., Masarie, K., et al. (2007). An atmospheric perspective on North American carbon dioxide exchange: CarbonTracker. *Proceedings of the National Academy of Sciences of the United States of America*, *104*(48), 18925–18930. https://doi.org/10.1073/pnas.0708986104

Kass, R. E., & Raftery, A. E. (1995). Bayes factors. *Journal of the american statistical association*, *90*(430), 773-795

Kitanidis, P. (1997). Introduction to Geostatistics: Applications in Hydrogeology, Stanford-Cambridge program, Cambridge University Press, Cambridge

Lu, T. T., & Shiou, S. H. (2002). Inverses of 2× 2 block matrices. *Computers & Mathematics with Applications*, *43*(1-2), 119-129. https://doi.org/10.1016/S0898-1221(01)00278-4

Luus, K. A., Commane, R., Parazoo, N. C., Benmergui, J., Euskirchen, E. S., Frankenberg, C., ... & Zona, D. (2017). Tundra photosynthesis captured by satellite-observed solar-induced chlorophyll fluorescence. *Geophysical Research Letters*, *44*(3), 1564-1573. https://doi.org/10.1002/2016GL070842

Mahadevan, P., Wofsy, S. C., Matross, D. M., Xiao, X., Dunn, A. L., Lin, J. C., ... & Gottlieb, E. W. (2008). A satellite-based biosphere parameterization for net ecosystem CO2 exchange: Vegetation Photosynthesis and Respiration Model (VPRM). *Global Biogeochemical Cycles*, *22*(2). https://doi.org/10.1029/2006GB002735

Masarie, K., Peters, W., Jacobson, A., & Tans, P. (2014). Obspack: a framework for the preparation, delivery, and attribution of atmospheric greenhouse gas measurements. *Earth Syst. Sci. Data*, 6 (2), 375-384. https://doi.org/10.5194/essd-6-375-2014

Michalak, A. M., Bruhwiler, L., & Tans, P. P. (2004). A geostatistical approach to surface flux estimation of atmospheric trace gases. *Journal of Geophysical Research D: Atmospheres*, *109*(14), 1–19. https://doi.org/10.1029/2003JD004422

Miller, S. M., Miller, C. E., Commane, R., Chang, R. Y. W., Dinardo, S. J., Henderson, J. M., et al. (2016). A multiyear estimate of methane fluxes in Alaska from CARVE atmospheric observations. *Global Biogeochemical Cycles*, *30*(10), 1441–1453. https://doi.org/10.1002/2016GB005419

Miller, S. M., Michalak, A. M., Yadav, V., & Tadié, J. M. (2018). Characterizing biospheric carbon balance using CO2 observations from the OCO-2 satellite. *Atmospheric Chemistry and Physics*, *18*(9), 6785–6799. https://doi.org/10.5194/acp-18-6785-2018

Miller, S. M., Saibaba, A. K., Trudeau, M. E., & Andrews, A. E. (2019). Geostatistical inverse modeling with very large datasets : an example from the OCO-2 satellite. *Geoscientific Model Development*, https://doi.org/10.5194/gmd-2019-185

Mueller, K. L., S. M. Gourdji, and A. M. Michalak (2008), Global monthly averaged CO_2 fluxes recovered using a geostatistical inverse modeling approach: 1. Results using atmospheric measurements, *J. Geophys. Res.*, **113**, D21114, doi:10.1029/2007JD009734

NOAA Carbon Cycle Group ObsPack Team(2018). INPE atmospheric carbon dioxide data for the period 2015-2017; obspack_co2_1_INPE_RESTRICTED_v2.0_2018-11-13; NOAA Earth System Research Laboratory, Global Monitoring Division.

http://dx.doi.org/10.25925/20181030

Randerson, J. T., Thompson, M. V., Conway, T. J., Fung, I. Y., & Field, C. B. (1997). The contribution of terrestrial sources and sinks to trends in the seasonal cycle of atmospheric carbon dioxide. *Global Biogeochemical Cycles*, *11*(4), 535-560.

Randerson, J.T., G.R. van der Werf, L. Giglio, G.J. Collatz, and P.S. Kasibhatla. (2018). Global Fire Emissions Database, Version 4.1 (GFEDv4). ORNL DAAC, Oak Ridge, Tennessee, USA. https://doi.org/10.3334/ORNLDAAC/1293

Raftery, A. E. (1995). Bayesian model selection in social research. *Sociological methodology*, *25*, 111-164.

Schwarz, G.: Estimating the dimension of a model, *Ann. Stat*., 6, 461–464, available at: http://www.jstor.org/stable/2958889, 1978.

Sweeney, C., Karion, A., Wolter, S., Newberger, T., Guenther, D., Higgs, J. A., ... & Miller, J. B. (2015). Seasonal climatology of CO2 across North America from aircraft measurements in the NOAA/ESRL Global Greenhouse Gas Reference Network. *Journal of Geophysical Research: Atmospheres*, *120*(10), 5155-5190. doi:10.1002/ 2014JD022591

Takahashi, T., Sutherland, S., and Kozyr, A. (2016). Global Ocean Surface Water Partial Pressure of CO2 Database: Measurements Performed During 1957–2015 (Version 2015), ORNL/CDIAC-160, NDP-088(V2015), Oak Ridge National Laboratory, U.S. Department of Energy, Oak Ridge, Tennesee, http://doi.org/10.3334/CDIAC/OTG.ND P088(V2015)

Thornton, P. E., Doney, S. C., Lindsay, K., Moore, J. K., Mahowald, N., Randerson, J. T., ... & Lee, Y. H. (2009). Carbon-nitrogen interactions regulate climate-carbon cycle feedbacks: results from an atmosphere-ocean general circulation model. *Biogeosciences*, *6*(10), 2099-2120.

Yadav, V., Mueller, K. L., & Michalak, A. M. (2013). A backward elimination discrete optimization algorithm for model selection in spatio-temporal regression models. *Environmental Modelling and Software*, *42*, 88–98. https://doi.org/10.1016/j.envsoft.2012.12.009.